Journal of Applied Physics ARTICLE scitation.org/journal/jap

Propagation of atmospheric pressure plasmas through interconnected pores in dielectric materials

Cite as: J. Appl. Phys. **129**, 143302 (2021); doi: 10.1063/5.0045706
Submitted: 28 January 2021 · Accepted: 20 March 2021 ·
Published Online: 9 April 2021

Juliusz Kruszelnicki,[1,a)] Runchu Ma,[2,b)] and Mark J. Kushner[2,c)]

AFFILIATIONS

[1]Nuclear Engineering and Radiological Sciences Department, University of Michigan, 2355 Bonisteel Blvd., Ann Arbor, Michigan 48109-2104, USA
[2]Electrical Engineering and Computer Science Department, University of Michigan, 1301 Beal Ave., Ann Arbor, Michigan 48109-2122, USA

Note: This paper is part of the Special Topic on Fundamentals and Applications of Atmospheric Pressure Plasmas.
[a)]jkrusze@umich.edu
[b)]runma@umich.edu
[c)]**Author to whom correspondence should be addressed:** mjkush@umich.edu

ABSTRACT

The propagation of atmospheric pressure plasmas (APPs) on and through porous dielectric materials is being investigated for plasma-catalysis and functionalizing biomedical materials for tissue scaffolding and bone regeneration. Such plasma functionalization improves wettability and cell attachment, and so uniformity of the treatment of the pore surfaces is important. The method of propagation of APPs through porous media is not well characterized. In this paper, we discuss results from a computational investigation of humid air APPs propagating through short fully interconnected pore-chains in a dielectric substrate. The properties of the dielectric and pores (diameter 150 μm) were chosen to resemble bone scaffolding. We found that photoionization is an important feature in plasma propagation through pore-chains to seed electrons in the following pore in the chain. This seeding of electrons in regions of high electric field allows for the formation of micro-streamers and surface ionization waves. This is particularly important when the openings between pores are small. The orientation of the pore-chain with respect to the applied electric field has a significant impact on plasma generation, mode of propagation, and fluences of short-lived, reactive species to the surfaces of the pores. The uniformity of fluences of charged and short-lived neutral species to the pore surfaces decreases as the angle of the pore chain deviates from being aligned with the applied electric field. Diffusion within pores improves the uniformity of fluences to pore surfaces for long-lived species on longer time scales compared to their post-discharge uniformity.

I. INTRODUCTION

Atmospheric pressure plasmas are an efficient source of charged particles, reactive neutral species, photons, and electric fields for treating surfaces for chemical processing and biomedical applications.[1–3] Atmospheric pressure plasmas (APPs) in the form of corona discharges and dielectric barrier discharges (DBDs) have long been used to functionalize polymers, both in batch mode and in web processing, to improve adhesion, and to increase the hydrophilic nature of the surface.[4–6] The use of APPs for functionalizing the surfaces of topologically complex materials—such as porous media—is less common. Porous materials have a wide range of applications, including their use as catalysts and catalyst substrates due to their high surface to volume ratio and high catalytic efficiency. Plasma interactions with these porous materials are being investigated, and studies to date have shown substantial synergetic effects.[7–12] Porous ceramics and polymers are also used as scaffolding in tissue engineering to enable, for example, the re-growth of bone structures and cell regeneration and for the growth of soft tissues.[4,13,14] The application of APPs has been shown to accelerate and stabilize the growth of cells on these scaffolds.[5,13,15–17]

Plasmas have also been shown to sterilize these porous materials and have been used for this purpose *in vivo* and *ex vivo* during dental procedures.[18] Plasmas have been utilized to functionalize and coat porous materials, demonstrating the ability to penetrate into the interior of foams and to affect the pore structure.[19–21]

The propagation of plasmas on the surface of porous materials has been experimentally investigated in both the catalysis and medical fields.[13,15,22–30] The complexity of the geometry presents many challenges.[26,31,32] Fluid and particle-in-cell (PIC) modeling of plasma propagation into micrometer-scale pores indicate that even in these small structures, transport is dominantly electric field-driven drift as opposed to diffusion. Due to the polarization of the pore materials and subsequent electric field enhancement, large electron densities were produced in the pores. While higher plasma densities near surfaces were observed, surface ionization waves were not observed suggesting that the higher plasma densities were due to secondary electron emission. Photoionization was not found to be impactful. Swanson and Kaganovich investigated secondary electron emission from foam-like or fuzz-like surfaces using Monte-Carlo simulations and analytical models.[33] They found that secondary electron yield decreases from foam-like and fuzz-like surfaces compared to planar surfaces. Gu *et al.* modeled surface discharges propagating into pores using PIC methods.[34] They found an enhanced plasma density near the interior surfaces of the pores compared to the volumetric discharge.

In this paper, we discuss results from two-dimensional (2D) simulations of plasma propagation through short chains of interconnected, 150 μm diameter pores in dielectric materials. The size and interconnectivity of these structures are similar to those found in tissue scaffolding.[25] We found that plasma propagation from pore-to-pore depends heavily on photoionization, which allows for seeding of electrons into regions of high electric fields in the next pore. The photoionization is particularly important when the opening between interconnected pores is small, a condition which decreases the ability of electrons and ions to follow electric field lines and continue propagating from pore to pore. The angle of the pore-chain with respect to the applied electric field is important to the manner of plasma propagation through the pore chain. Propagation changed from being dominated by microdischarges for vertically oriented pore-chains to surface ionization waves (SIWs) for pore-chains oriented at an angle. Depending on the angle of the pore-chains, fluxes of short-lived species (e.g., ions, electrons, hydroxyl radicals, electronically excited states) to the inside surface of the pores were preferentially onto one side of the pore-chain. This asymmetry in incident fluxes did not occur for long-lived species (e.g., ozone, hydrogen peroxide, acids) over longer time scales, as diffusive transport in the pores during the afterglow following a discharge pulse homogenizes the fluxes.

A review of the model and description of the initial conditions are in Sec. II. A discussion of the plasma dynamics in the base-case, a vertically oriented pore-chain, is in Sec. III. The influence of the size of openings between pores is discussed in Sec. IV. Plasma properties in pore-chains having an angle with respect to the applied electric field are discussed in Sec. V. Concluding remarks are given in Sec. VI.

II. DESCRIPTION OF THE MODEL AND INITIAL CONDITIONS

The plasma modeling platform used in this investigation is *nonPDPSIM*, which is described in detail in Ref. 35. Only a short overview of the model will be given here. *nonPDPSIM* is a two-dimensional plasma hydrodynamics simulator that simultaneously integrates Poisson's for the electric potential and continuity equations for charged species on an unstructured numerical mesh. The form of Poisson's equation solved is

$$-\nabla \cdot \varepsilon \nabla \Phi = \sum_i q_i n_i + \rho_m, \tag{1}$$

where Φ is the electric potential, ε is the permittivity, q_i is the charge of species i having density n_i, and ρ_M is the charge on surfaces and in materials. The continuity equation for charged particles is

$$\frac{\partial n_i}{\partial t} = -\nabla \cdot \vec{\Gamma}_i + S_i - \left[\sum_m \nabla \cdot \vec{\Gamma}_m \gamma_m + \sum_k \nabla \cdot \vec{\varphi}_k \delta_k \right], \tag{2}$$

where Γ_i is the flux of species i. The source due to collisions is S_i. At mesh points adjacent to solid surfaces, secondary electron emission and photoemission emission are also included (bracketed terms). Here, γ_m is the secondary electron emission coefficient of species m, and φ_k is the flux of photon k incident onto the surface with the photoelectron emission coefficient δ_k. Fluxes of charged particles are given by the Scharfetter–Gummel method that automatically provides fluxes as either upwind or downwind. Transport of neutral species is solved using diffusion equations.

The electron temperature is obtained by integrating the energy conservation equation

$$\frac{\partial}{\partial t}\left(\frac{3}{2} n_e k_B T_e\right) = S_P(T_e) - L_P(T_e) - \nabla \cdot \left(\frac{5}{2} \vec{\Gamma}_e k_B T_e - \kappa_e(T_e) \nabla T_e\right), \tag{3}$$

where T_e is the electron temperature, n_e is the electron density, k_B is Boltzmann's constant, κ is the electron thermal conductivity, S_P is the source of power, in this case, Joule heating from the electric field, and L_P represents collisional losses or gains in energy. Electron temperatures are spatially resolved at each node in the unstructured, static mesh. Electron impact rate and transport coefficients as a function of mean electron energy are obtained from look-up tables produced by stationary solutions of Boltzmann's equation for the electron energy distribution.

Radiation transport is addressed by employing a Green's function for photons emitted at each numerical mesh node and propagating to a set of neighboring nodes within its line-of-sight. The flux of photons between the emitting and neighboring nodes decreases by the isotropic spherical expansion of the initially emitted photons, by absorption by intervening species, or by obscuration by structures. Photoionization of O_2 by photons emitted by

excited nitrogen species [$N_2(b^1\Pi)$ and $N_2(b^1\Sigma)$] was included with a cross section of 1.5×10^{-17} cm^2.

All ions neutralize when striking surfaces and electrons have unity sticking coefficient, both processes resulting in charging of the surface. All electronically excited states quench to their ground states with unity probability except for metastable states of homo-nuclear diatomic molecules that have lower quenching probabilities. The quenching coefficient of $O_2(^1\Delta)$ is 0.02 and that of $N_2(A)$ is 0.05. The quenching coefficients are unity for vibrationally excited species that are infrared-active, whereas those for homo-nuclear, non-infrared active species are lower. The quenching coefficient of $O_2(v)$ is 0.02 and that of $N_2(v)$ is 0.05.

During the inter-pulse pulse period, the neutral plasma option was utilized. When the voltage is turned off, Poisson's equation is no longer solved. Plasma neutrality is enforced by setting electron densities equal to the difference between the positive and negative ion densities, and setting the electron temperature equal to the gas temperature (At atmospheric pressure, the electron thermalization time is only a few nanoseconds.). The transport of ions is then given by their thermal transport coefficients since there is no electron-mediated ambipolar enhancement to rates of diffusion. Although the solutions for charged and neutral transport are implicit, there are still limits to the time steps that can be taken, for example, not exceeding multiplicative factors of the dielectric relaxation time or the Courant limit, or times to deplete species by reactions. The time step in the afterglow is determined primarily by the processes having the fastest rate of chemical reactions for depleting a species. In this study, the typical dynamically chosen time steps during the plasma period were about 1 ps, while the time steps in the neutral period following the discharge pulse started at 10^{-9} s and were incrementally increased to 10^{-6} s.

The base case has initial conditions of 300 K and 760 Torr (1 atm). The gas is humid air ($N_2/O_2/H_2O = 78/21/1$). Due to the short timescales in this study, gas heating was not considered. The reaction mechanism contains 67 species and 1512 reactions. The reaction mechanism is a modified version of that discussed in Ref. 36 taking into account only gas-phase species and eliminating several higher order positive and negative water cluster ions.

The base case geometry and the numerical mesh are shown in Fig. 1. Nominally, the geometry is a coplanar dielectric barrier discharge reactor with a 1 mm gap. The bottom dielectric is 740 μm in height and is meant to represent the type of porous ceramic that is used for bone scaffolding having a dielectric constant of 61.[37,38] The secondary electron emission coefficient for ions incident on the dielectric was 0.1. A chain of four vertically oriented interconnected circular pores open to the gas gap was placed in the dielectric. Each pore has a diameter of 150 μm and an inter-pore opening of 50 μm.

The plasma conditions were the same for all cases. A −8 kV pulse was applied to the top electrode, while the bottom electrode was held at ground potential. The voltage pulse has a total duration of 10 ns. The voltage rises linearly from 0 to −8 kV in 5 ns and is held at −8 kV for an additional 5 ns before being brought to zero in a step function manner. A plasma seed with a peak density of 1×10^{10} cm^{-3} and a radius of 100 μm was placed directly above the pore-chain opening near the top electrode to initialize the discharge. Following the 10 ns voltage pulse, a 10 ms afterglow period was simulated assuming quasi-neutral conditions. All surfaces are initially uncharged. So these results address either the first discharge pulse through the porous network or a low enough pulse repetition rate that the majority of surface charge will have dissipated prior to the next pulse.

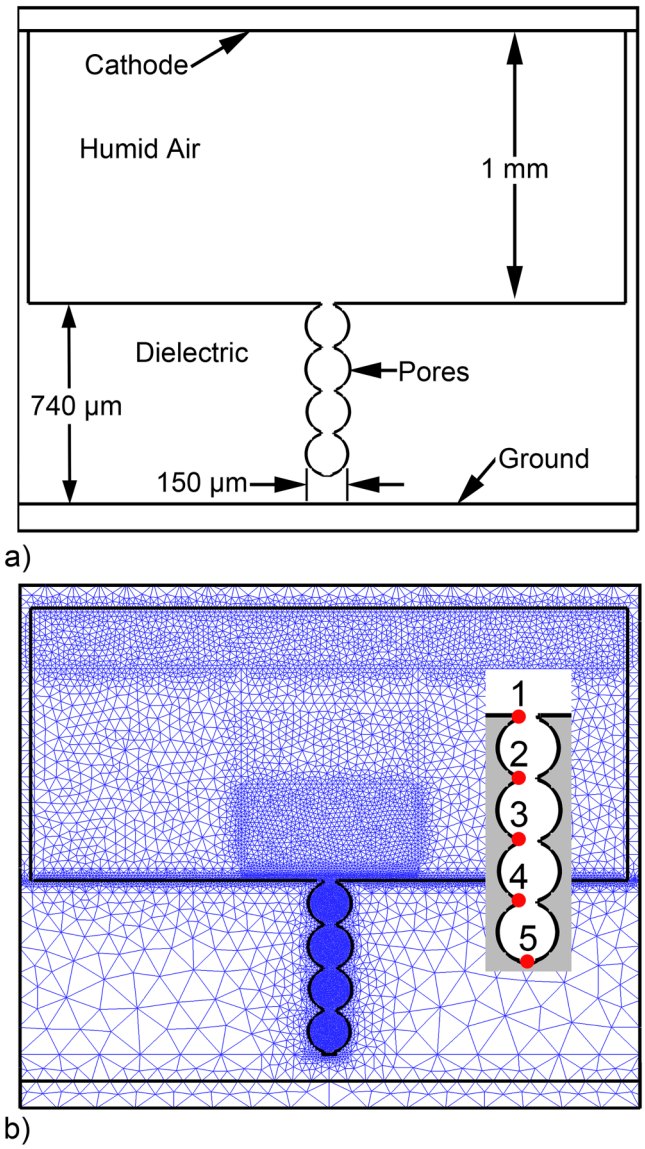

FIG. 1. Geometry for the base case. (a) Schematic of the computational domain. (b) Numerical mesh. Four pores with diameters of 150 μm with 50 μm openings are embedded into a 600 μm thick dielectric. The powered electrode is located 1 mm above the dielectric. The numbers in the inset identify locations that fluences are collected in later figures.

III. PLASMA PROPAGATION INTO VERTICAL PORE-CHAINS

The evolution of the electron density as a function of time is shown Fig. 2(a) for a discharge pulse above a vertical pore chain. An enlargement of the pores with electron density is shown in Fig. 2(b). The times noted in all figures are relative to the beginning of the voltage pulse. Note that the scales of the contours are changed between frames. Upon the application of voltage, the electron density drifts downward—reminiscent of a Townsend avalanche—as shown in Fig. 2(a) at 3 ns. Once the electrons intersect with the surface of the lower dielectric (5 ns, $n_e \approx 2 \times 10^{10}$ cm^{-3}), the surface charges negatively, which launches a positive space-charge streamer traveling upward toward the cathode (8 ns). The streamer head has a moderately high electron temperature ($T_e \approx 10$ eV) and is electropositive ($\rho/q \approx 10^{14}$ cm^{-3}). In crossing the 1 mm gap, the electron density in the head of the streamer reaches 3×10^{15} cm^{-3}. Once the microdischarge bridges the gap back to the cathode, the impedance of the plasma column is low, transferring the cathode potential to the surface of the dielectric. This transfer of potential to the surface produces sufficient intense lateral electric fields to launch surface ionization waves (SIWs) across the top of the dielectric [Fig. 2(a) at 9.3–9.8 ns]. The electron temperature in the leading portion of the SIW is approximately 5 eV, producing electron densities of 7×10^{14} cm^{-3}. The transfer of the cathode potential to the surface of the dielectric and to the top of the pore chain also launches an electron avalanche into the pores.

The time evolution of the electron density through the pore-chain is shown in Fig. 2(b). Time sequences of plasma properties in the second pore from the top of the chain are shown in Fig. 3—displaying the electron source by photoionization, ionization source by electron impact, electric field/gas number density (E/N), and electron density (Note that in the enlarged images of the pores, the contour scale was chosen to emphasize plasma properties inside the pore of interest. As a result, the contour scale may be saturated outside the pore where values exceed the maximum of the plotted scale.). The plasma is initially seeded in the topmost pore by photo-ionization from the bulk plasma above the pore opening. These seed electrons then drift and avalanche in the applied axial electric field, intensified by the polarization of the adjacent curved

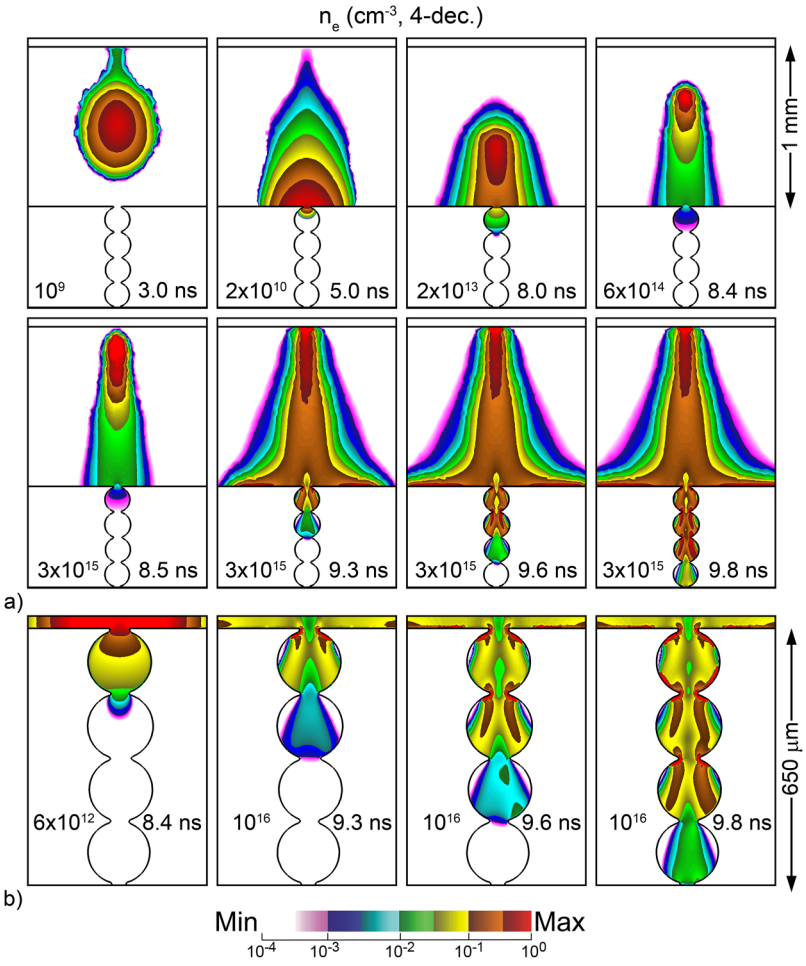

FIG. 2. Time evolution of electron density in the base case plotted over 4 decades on a long-scale. (a) Streamer in the gas phase and pore-chain. (b) Enlargement of the pore-chain. The maximum value and time of the image are noted in each frame.

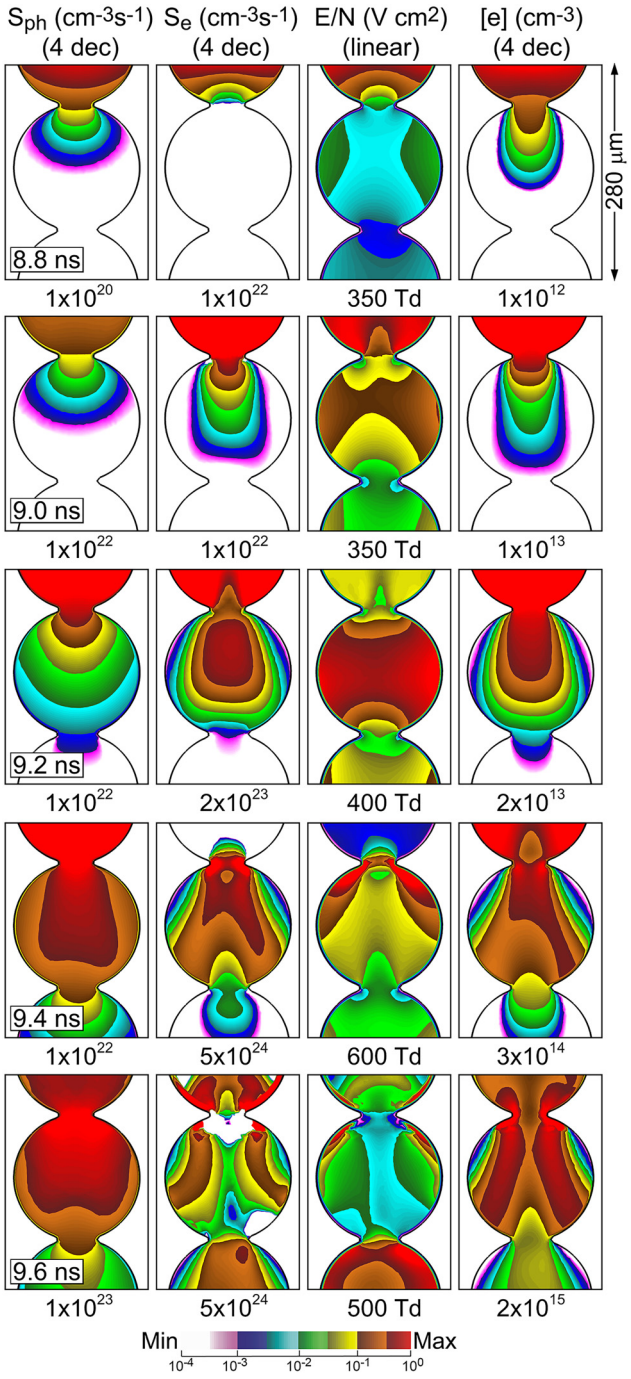

FIG. 3. Time sequence (top to bottom) of plasma properties in the second pore from the top of the pore chain. (left to right) Photoionization source (S_{ph}), electron impact ionization source (S_e), electric field/gas number density (E/N), and electron density ([e]). Except for E/N, quantities are plotted on a 4-decade log-scale. The maximum value in each image is noted below the frame. The ranges of the values plotted were chosen to emphasize plasma properties in the pore of interest. This resulted in some images being saturated in the pore above.

dielectric surfaces. Initiation of the plasma from pore-to-pore along the chain is dominated by photoionization.

In this orientation of the pores, the sharply rounded edges of the pore openings are in the horizontal direction. With the applied electric field oriented vertically, the polarization of the dielectric produces a minimum in the electric field in the horizontal direction at the edges. There is a maximum in electric field in the vertical direction above and below the edges of the pore openings. Once photoionization seeds electrons inside the pore, electron avalanche begins to dominate and particularly so in the polarized intensified electric fields below the edges of the openings. Ionization waves (IWs) are launched from those locations on each side of the pore from these locations of electric field enhancement. Electron densities up to 2×10^{15} cm^{-3} are produced inside the pore.

The electron avalanche in the pores tends to follow the electric field lines (in the downward direction) and negatively charge the bottom surfaces of the pores. The upper surfaces of the pores become positively charged. This results in the formation of E/N of up to 600 Td (1 Td = 10^{-17} V cm^2), allowing for the formation of SIWs along the walls of the pores. Formation of SIWs is important for the surface functionalization of the porous media as it enables production of short-lived, reactive species and VUV photons to reach the surface. The formation of SIWs in pore-like structures was also reported by Gu *et al.*[34] This process of seeding of electrons by photo-ionization through the narrow pore opening, followed by the formation of plasma filaments, and finally, SIWs continue in each of the consecutive pores.

In principle, the propagation of plasma through the vertically oriented pores should be symmetric across the mid-plane. The structures appearing in Figs. 2 and 3 are not perfectly symmetric. This lack of symmetry is due, in part, to the plasma entering the pore being slightly asymmetric and the numerical mesh not being perfect mirror-images on either side of the pore. In the extremely large electric fields (E/N > 500 Td) produced inside the pores, avalanche times are as short as tens of ps, which rapidly amplify small differences in E/N of only a few Td.

The fluences (time-integrated fluxes) of charged species (electrons, N_2^+, and O_2^+) and reactive oxygen and nitrogen species, RONS (NO, OH, H_2O_2, and O_3) to the inside surfaces of the pores and the top surface of the dielectric after the discharge pulse at 10 ns are shown in Figs. 4(a) and 4(b). The peaks in fluences numbered in Fig. 4(a) correspond to the pore openings and bottom of the last pore as labeled in Fig. 1(b). The bottom of the pore-chain is located between the dotted lines in Fig. 4. Moving left and right from the center is the equivalent of moving upward along the inside surface of the left and right side of the pore-chains and finally out the top of the pore. During the short discharge pulse, fluences to the surfaces are dominated by species produced within a few to tens of micrometers of the surface. Even on these short timescales, there is significant ion chemistry that occurs. For example, in atmospheric pressure air plasmas, the three-body reaction that converts N_2^+ to N_4^+ occurs within a few nanoseconds. Over the 10 ns duration of the voltage pulse, the majority of the gas phase N_2^+ that does not charge exchange with other species, is converted to N_4^+. The end result is that both the magnitude and shape of the fluence of N_2^+ and N_4^+ to the pore surfaces are nearly the same.

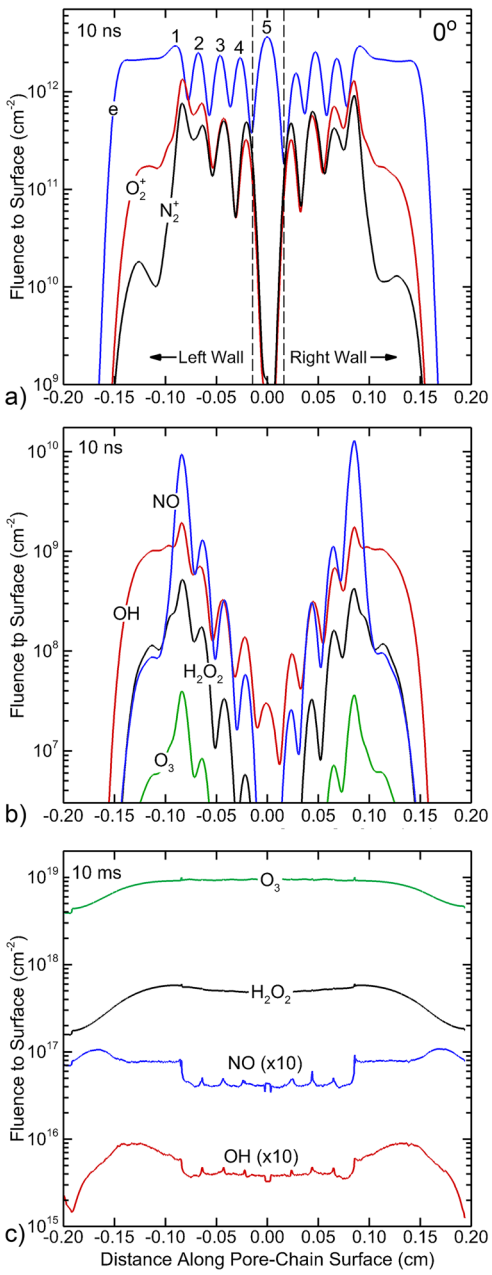

FIG. 4. Fluences of plasma-generated species to the inside surfaces of the vertically oriented pore-chain. (a) Electrons and ions after 10 ns, (b) neutral species after 10 ns, and (c) neutral species after 10 ms. The maxima in fluences correspond to the pore openings. The numbering of the peaks correlates with locations cited in Fig. 1. The dotted lines are the boundaries of the floor of the bottom pore.

The fluences of both charged species and neutral RONS are symmetrical to both sides of the pore-chain after the discharge pulse. The local maxima in fluences correspond to the pore openings where electric field enhancement leads to higher plasma densities. The minima in fluences between the peaks correspond to the curved walls of the pores and the weaker SIWs that propagate along the walls. After 10 ns, the larger fluences of electrons compared to positive ions result from the negative polarity of the discharge that negatively charges the anode-covering dielectric surfaces. The fluences of charged species are higher than those of neutrals ($2–3 \times 10^{12}$ cm^{-2} compared to $7–8 \times 10^{10}$ cm^{-2}). For the same densities, fluxes of charged particles to surfaces are higher than the neutral RONS either due to drift in the applied electric field (electrons) or due to the ambipolar electric field (ions).

The lower fluences of neutral RONS can also be attributed to the reaction sequence required for their creation. The production of O_3, NO, and H_2O_2 requires additional gas phase reactions following the generation of primary radicals by electron impact dissociation (e.g., O, N, and OH). These additional reactions simply take time to occur, and so these species have not built up large densities and fluences during the discharge pulse. Fluences are generally lower deeper into the pore-chain. This results from a general decrease in plasma density down the pore chain and shorter time for fluxes to reach the surface.

During the afterglow following the discharge pulse, neutral species produced in the interior of the pores have time to diffuse to the surfaces, and post-pulse chemistry takes place to either deplete species or generate new species. The fluences of neutral RONS to the pore surfaces 10 ms after the discharge pulse are shown in Fig. 4(c). The uniformity of the fluences of neutral RONS is greatly improved and greatly increased compared to their post-pulse values, though not in direct proportion to their post-pulse values. The improved uniformity and larger fluences are due to the slower diffusion of the neutral species from the volume of the pores to the surfaces, and the fact that low-reacting species with the surfaces will simply accumulate fluence over time.

To allow for some moderate depletion of species during the afterglow, we specified a reaction probability on the surfaces of 0.01 for O_3, H_2O_2, NO, and OH. These reaction probabilities should be interpreted as rates of consumption of these species on surfaces. The changes in relative values of the fluences at 10 ms compared to the post-discharge values at 10 ns are due to the gas phase reactivity consuming or generating these species. For example, after 10 ms, O_3 (10^{19} cm^{-2}) and H_2O_2 (5×10^{17} cm^{-2}), which require additional collisions to form, have the largest fluences, whereas after the discharge pulse at 10 ns, they had the lowest fluences. After 10 ms, NO ($4–5 \times 10^{16}$ cm^{-2}) and OH ($3–4 \times 10^{15}$ cm^{-2}) have the smallest fluences, whereas after the discharge pulse at 10 ns, they had the largest fluences. Species formed due to electron impact dissociation produce large fluences after the discharge pulse, such as OH. However, these species also tend to be more reactive in the gas phase, being consumed in forming more stable species, such as H_2O_2. These reactions lower the fluences of the reactive primary species while increasing the fluences of the more stable product(s).

Surface reactivity is important in assessing these fluences since the surface to volume ratio is large for small pores. Surface sites have a density of about 10^{15} cm^{-2}, and so the cylindrical pores considered here having a diameter of 150 μm have about 4.7×10^{13} sites per centimeter of depth. These dimensions require a gas phase radical density of 2.7×10^{17} to enable the gas phase species to react

TABLE I. Surface-averaged fluences of reactive species to the pore-chain walls.

Species	Average fluence (cm^{-2}) at 10 ns	Average fluence (cm^{-2}) at 10 ms	Fraction surface sites reacted
Short-lived species			
$N_2(A)$	1.1×10^{12}	7.2×10^{12}	1.1×10^{-7}
$N_2(v)$	7.4×10^{11}	1.4×10^{14}	2.2×10^{-6}
O_2^+	2.0×10^{11}	3.7×10^{13}	6.3×10^{-7}
O	1.4×10^{11}	2.5×10^{16}	3.0×10^{-3}
OH	3.8×10^{8}	1.3×10^{15}	4.8×10^{-6}
N	1.4×10^{11}	6.3×10^{14}	7.0×10^{-6}
N_2^+	1.3×10^{11}	6.0×10^{12}	9.5×10^{-8}
N_4^+	1.1×10^{11}	1.8×10^{12}	4.0×10^{-8}
$O_2(v)$	6.1×10^{10}	2.5×10^{13}	4.2×10^{-7}
N_2^{**}	3.3×10^{10}	7.6×10^{11}	1.2×10^{-8}
$O_2(^1\Delta)$	2.3×10^{10}	7.6×10^{16}	1.3×10^{-3}
N_3^+	1.1×10^{10}	1.3×10^{12}	2.5×10^{-8}
Long-lived species			
O_3	3.4×10^{6}	5.2×10^{18}	1.1×10^{-1}
H_2	1.1×10^{8}	1.4×10^{18}	5.3×10^{-3}
HNO_2	2.6×10^{5}	6.7×10^{17}	1.6×10^{-2}
N_2O_5	4.0×10^{-3}	4.0×10^{17}	1.2×10^{-3}
H_2O_2	6.1×10^{7}	2.5×10^{17}	4.6×10^{-3}
HNO_3	1.0×10^{3}	1.7×10^{17}	4.0×10^{-3}
HO_2NO_2	1.1×10^{-2}	8.0×10^{16}	2.3×10^{-3}
N_2O	5.2×10^{8}	6.0×10^{16}	7.9×10^{-3}
NO_2	6.1×10^{7}	1.9×10^{16}	4.5×10^{-4}
NO	4.7×10^{8}	6.3×10^{15}	1.0×10^{-4}

with (and be consumed by) every surface site. The details of this reactivity with the surface are unique to each material.

The fluences of species to the walls of the pore-chain at 10 ns and 10 ms are listed in Table I. During the discharge pulse, the fluences are dominated by excited nitrogen species because of the composition of the gas (78% N_2). This leading fluences are followed by the fluences of ionized oxygen (ionization potential ≈12 eV), atomic oxygen (dissociation energy ≈5 eV), and nitrogen atoms (dissociation energy ≈12 eV). As the discharge transitions to an afterglow, species requiring additional (and possibly multiple) reactions to form begin to dominate. In particular, O_3, H_2O_2, and acids (HNO_x) form over many milliseconds. To provide some context for surface reactions and functionalization of porous materials, we assumed a surface reaction probability of 0.01 for all neutral species. With this reaction probability, the fraction of surface sites that are functionalized during the afterglow of the discharge pulse, also listed in Table I, ranges from 0.1 for O_3 and 0.004 for HNO_3 to as small as 1×10^{-4} for NO. With few exceptions, tens to hundreds of discharge pulses would be required to functionalize the entire inner surface of the pores.

IV. IMPACT OF INTER-PORE OPENING SIZE

The transport of species pore-to-pore is, in part, determined by the size of the opening between the pores. To investigate the consequences of this interconnectivity, the diameter of the openings between the pores, d_p, was varied from 37 to 150 μm. The diameter of the pores was held constant at 150 μm, meaning that the largest of the opening sizes produces a via or a trench. The evolution of electron densities with these pore openings is shown in Fig. 5.

As the size of pore openings decreases, the convective transport of electrons through the openings becomes progressively hindered by the charging of the pore surfaces in the vicinity of the opening, which in turn creates a space-charge barrier. As a result, the propagation of the discharge from pore-to-pore becomes progressively more dependent on photoionization to seed plasma in the next pore as the opening narrows. As the pore opening decreases in size, the electric field enhancement below the opening becomes more pronounced. Once there is plasma seeded in a lower pore, this more intense electric field enhancement launches micro-streamers across the pores. With the smallest opening ($d_p = 37\,\mu$m), the micro-streamers largely miss the sidewalls, and there is no SIW that propagates in a restrike fashion. As d_p increases, the electric field enhancement at the edges of the opening becomes directed more along the surface, and the plasma becomes more surface-hugging. At $d_p = 150\,\mu$m with straight walls, the plasma propagates along the surfaces of the trench as singular SIWs, being dependent on the self-generated electric field in the heads of the ionization front (peaking at E/N ≈ 420 Td, $T_e \approx 7$ eV) instead of geometric electric field enhancement. While the plasma does not uniformly fill the trench, fluxes of reactive species to the surface will be uniform due to the complete plasma coverage.

The propagation of the plasma through the pore chain slows as the pore opening d_p increases. This is a counter-intuitive result. The small radii of curvature of the dielectric produces a larger surface capacitance that, in principle, should require a longer dwell time of the plasma to fully charge. By this logic, the speed of propagation of the discharge should slow as d_p decreases. However, in order to obey this scaling, the plasma should propagate dominantly as an SIW whose motion is determined by the charging of the underlying capacitance of the surface. Instead, the SIW detaches from the surface as d_p decreases, a process that is just beginning to occur with $d_p = 112\,\mu$m. The evolution of the ionization wave from an SIW into a volumetric streamer eliminates the need for surface charging for the ionization to propagate and so reduces the dependence of discharge propagation on the specific capacitance of the surface.

The fluences of electrons, O_2^+, and N_2^+ to the pore surfaces during the voltage pulse for pore openings of 37, 75, 112, and 150 μm are shown in Fig. 6 (The fluences for a pore opening of 50 μm are in Fig. 4.). As the pore opening decreases in size, the convective charged particle transport through the opening decreases while the electric field enhancement at the edges of the opening increases. These trends result in more localized ionization near the openings, the launching of micro-streamers, and less intense SIWs. These combined effects produce more modulation in the charged particle fluences to the surfaces. With increasing pore opening, the local modulation in fluences decreases—that is, the fluences are locally more uniform. However, globally the fluences are less uniform with larger pore opening. This less uniform global uniformity is due to the decrease in speed of propagation of the

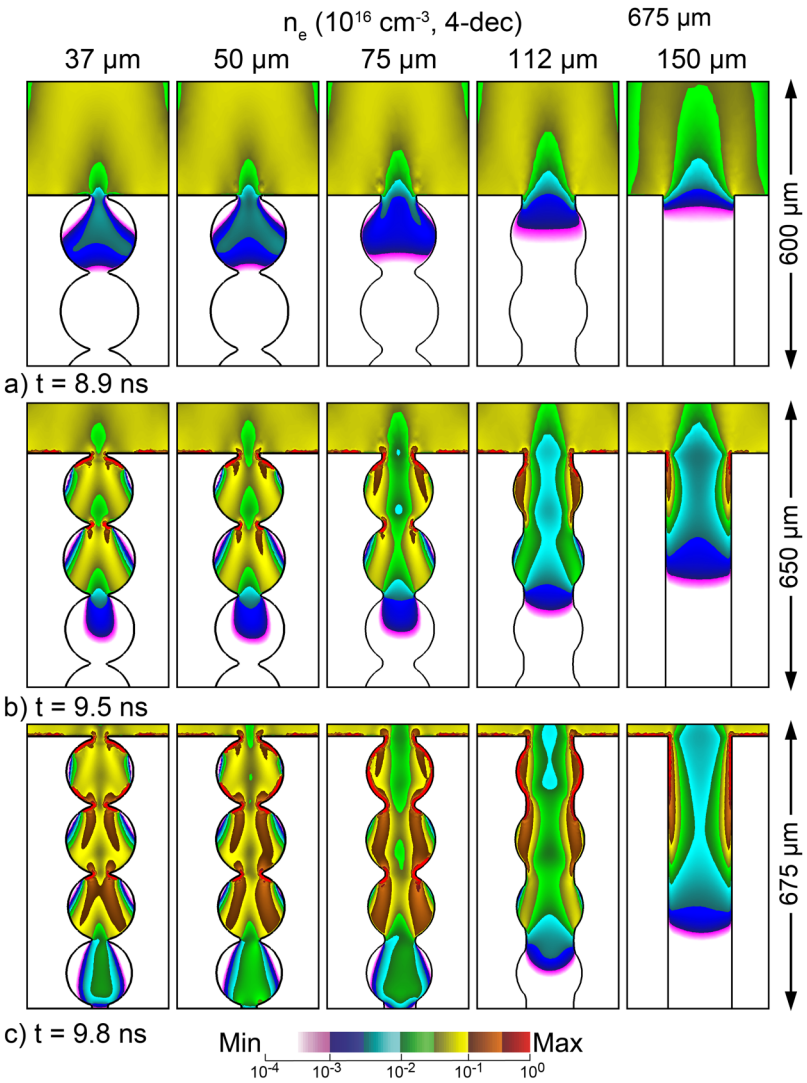

FIG. 5. Time sequence of electron density in pore-chains with varying pore-opening sizes (left to right) of 37, 50, 75, 112, and 150 μm. (a) 8.9 ns, (b) 9.5 ns, and (c) 9.8 ns, plasma formation becomes surface-discharge dominated as the openings become larger. The density is plotted on a log-scale over 4 decades.

plasma through the pores. For example, as noted, the plasma does not reach the bottom of the feature for the 150 μm opening.

V. ANGLE OF THE PORE-CHAIN

In actual porous material, the orientation of the pores with respect to the applied electric field is random, as is the manner of their interconnectivity. To investigate the consequences of the orientation of the pore-chain on discharge propagation, the angle of the pore-chain with respect to the surface normal of the electrodes was varied—0°, 22.5°, and 45.0°. The time evolution of electron density for these orientations is shown in Fig. 7. The electron impact ionization source and E/N in the third pore for the chain oriented at 45° are shown in Fig. 8. The plasma cascades though the pores in a different fashion as the angle moves away from the vertical. For all angles, photoionization is required to seed electrons in the next pore due to the constricting opening that limits electron transport. With an increasing angle of the pore chain, the opening between pores is more aligned with the applied electric field. This alignment produces polarization-induced electric field enhancement at the tips of the openings, as shown in Fig. 8(a). The electric field at the tips of the opening reaches values as high as 1000 Td for an orientation of 45°. Recall that for vertically oriented pores, there is instead a reduction in E/N at the tips of the opening. This progressive increase in E/N with increasing angle produces ionization in the pore opening directly adjacent to the surface, whereas with a shallow angle, the ionization is largely in the volume.

With the applied electric field progressively more normal to the walls of the pore chain with increasing angle, and with ionization occurring more adjacent to the surface, the plasma becomes increasingly asymmetric. The lower surfaces of the pores are charged negatively, a condition that supports SIWs that propagate

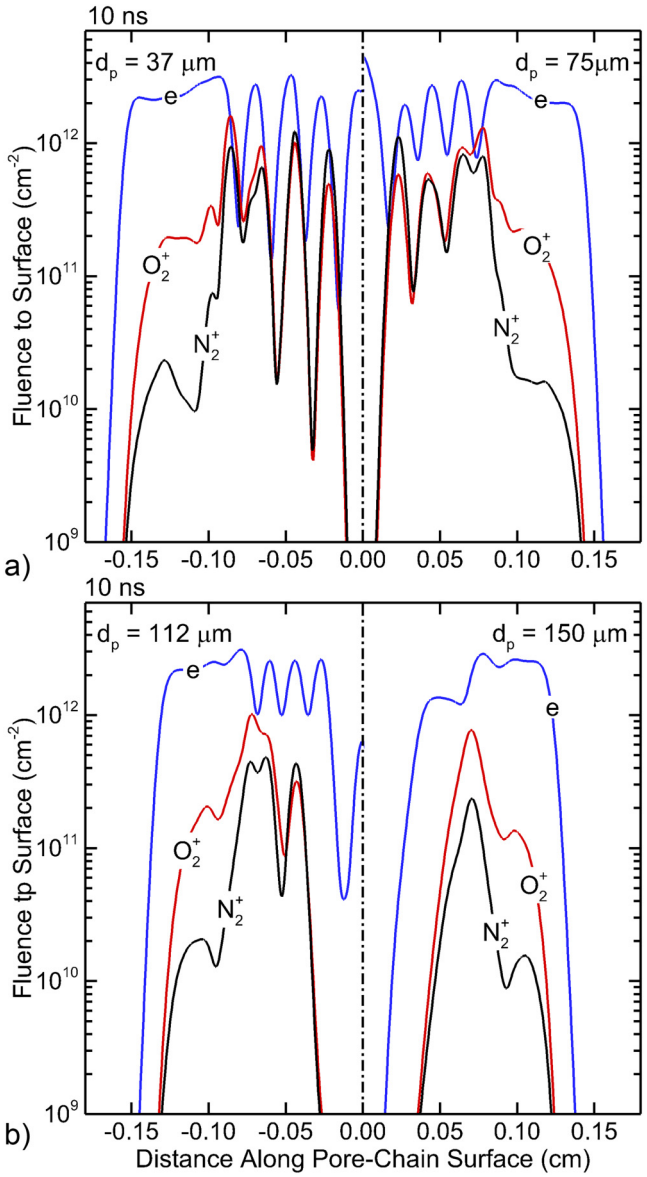

FIG. 6. Fluences of electrons and ions after 10 ns to the inside surfaces of the vertically oriented pore-chain for different pore openings. (a) 37 and 75 μm and (b) 112 and 150 μm. For each opening, the fluences are shown for only one wall (left or right). The maxima in fluences correspond to the pore openings.

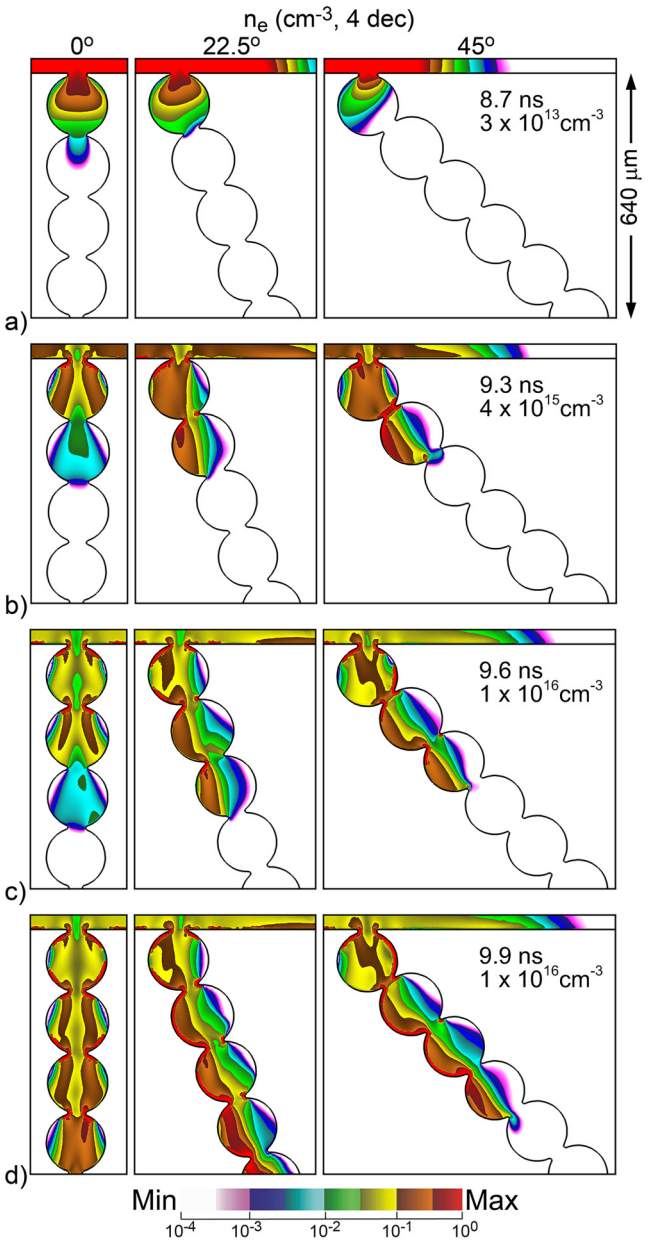

FIG. 7. Time sequence of electron density in pore-chains with varying angles (left to right) of 0°, 22.5° and 45°. (a) 8.7 ns, (b) 9.3 ns, (c) 9.6 ns, and (d) 9.9 ns, Plasma formation becomes surface-discharge dominated as the angle increases. The electron density is plotted on a log-scale over 4 decades. The maximum value for each time is noted in the third frame.

along the surface shown by the region of positive electron source and high E/N in Fig. 8. The trailing plasma column has densities reaching 2×10^{16} cm^{-3} with commensurately high conductivities that reduce E/N below self-sustaining. The electron source terms in the plasma column along the surface then become negative, dominated by attachment and recombination. With the charging of the lower surface of the pore, a positive SIW is launched upward along the top surface of the pore. However, this SIW stalls due to the shorting of the electric potential by the conductive plasma on the bottom surface. The end result is that as the angle of the pore-chain increases from the vertical, the discharge through the chain becomes progressively dominated by SIWs along the lower surface.

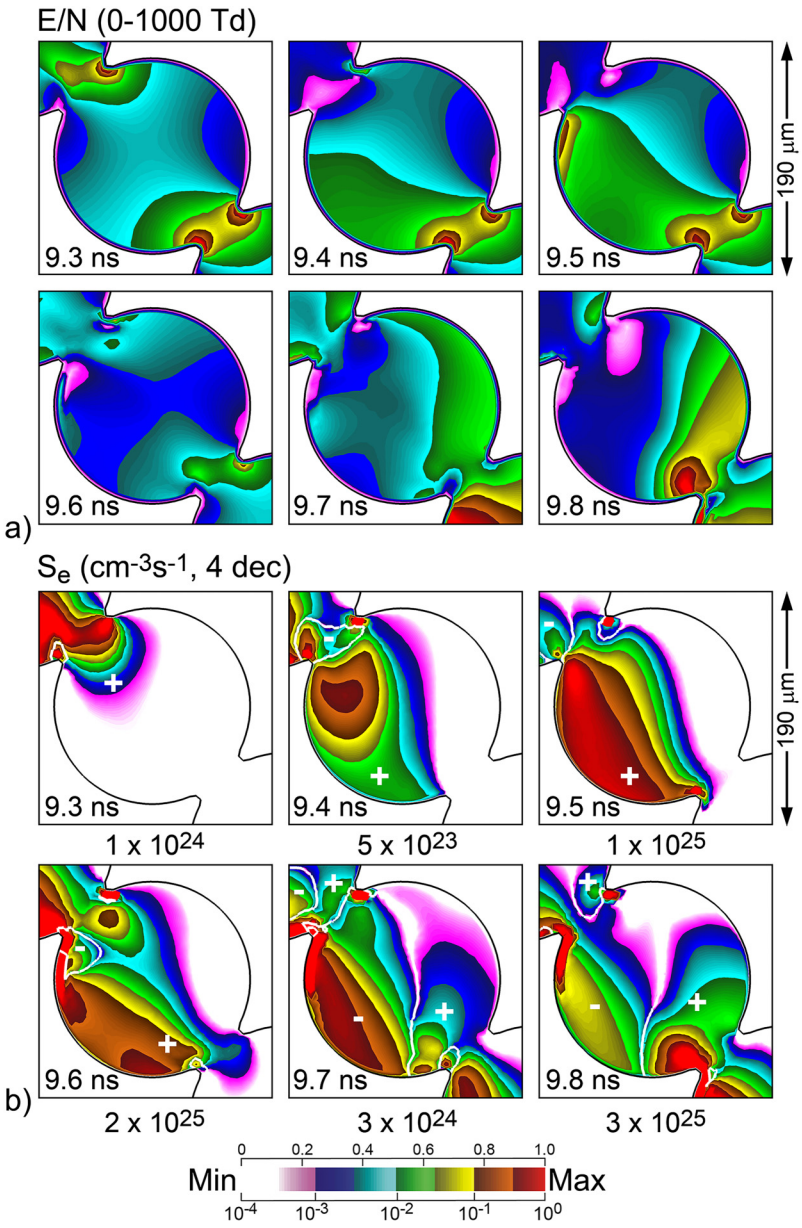

FIG. 8. Time sequences of plasma properties in the third pore in the pore-chain oriented at 45°. (a) E/N on a linear 0–1000 Td scale. (1 Td = 10^{-17} V cm^2). (b) Electron impact ionization source plotted on a 4-decade log-scale with the maximum value noted below each frame. The absolute value of the ionization source is plotted, with white lines separating the regions of electron impact producing positive gains in electron density (noted with "+") and regions in which electron impact produces losses (noted with "–").

The speed of propagation of SIWs depends, in part, on the effective surface capacitance (C_s, F/cm^2). As discussed earlier, SIWs propagating on surfaces with larger C_s tend to propagate slower. The volumetric ionization waves are much less sensitive to C_s of nearby surfaces. With increased C_s due to the orientation of the pores and a more SIW dominated plasma, the discharge in the pores at larger angle propagates slower.

The orientation of the pore chain imbedded in the dielectric affects the discharge propagation in the gas gap above the dielectric in at least two ways. The first is that the effective surface capacitance at the top of the dielectric is a function of the material density and layout below the surface. With the vertically oriented pore-chain, C_s is the same on both sides of the centerline. As the pore-chain angles to the right of the center, C_s increases on the right side relative to the left side. The second is that as the pore-chain fills with conductive plasma, the electric potential is shorted, bringing the cathode potential toward the top of the pore-chain. With increasing angle of the pore-chain and an asymmetric subsurface conductivity, the potential is arrayed asymmetrically above the dielectric.

For example, the electron density and electric potential at the end of the voltage pulse are shown in Fig. 9 for pore-chains

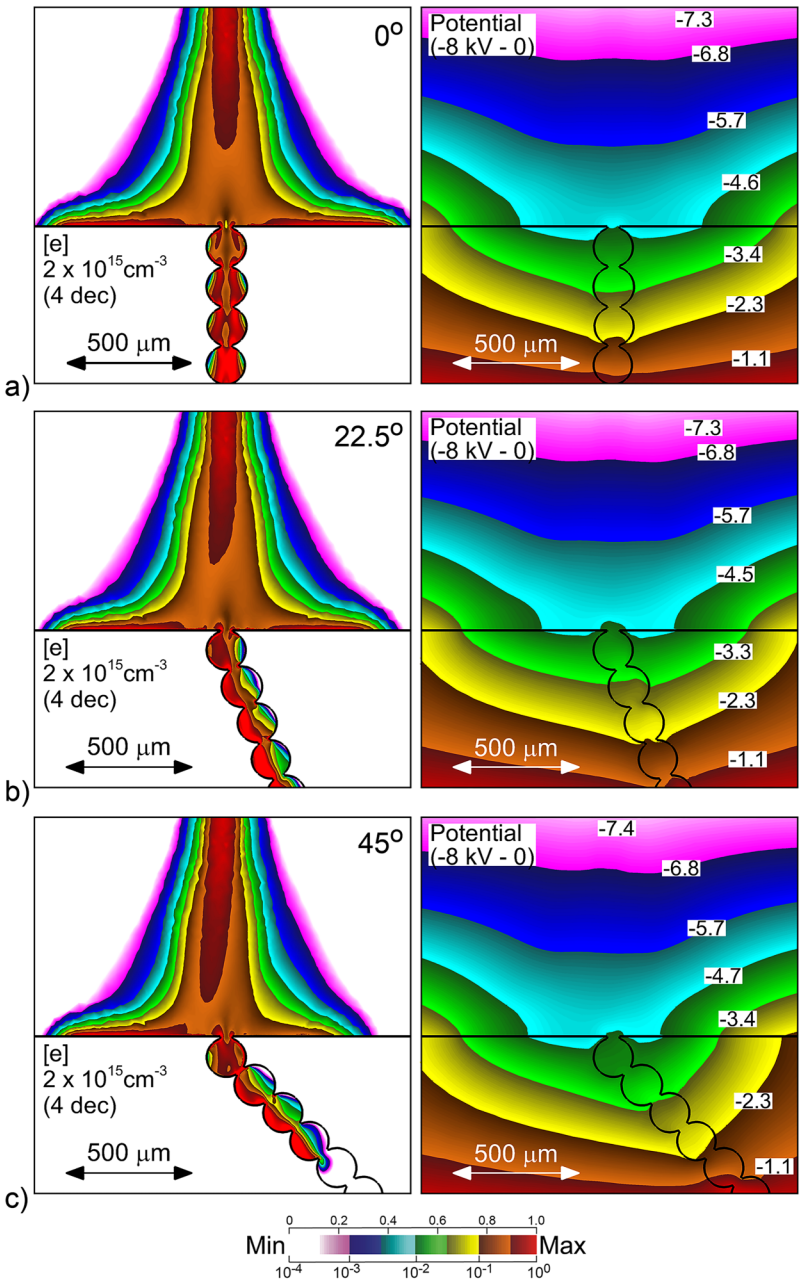

FIG. 9. Electron density and electric potential at the end of the discharge pulse for pore-chains at different angles. (a) 0°, (b) 22.5°, and (c) 45°. Electron density is plotted on a 4-decade log scale. Contour labels for electric potential have units of kilovolt.

oriented at 0°, 22.5°, and 45°. With the pore-chain at 0°, the micro-discharge streamer in the gap is essentially symmetrically arrayed above the pore-chain. The SIWs propagate with equal speeds to the right and left of the pore chain opening. The conductive plasma in the pore-chain reduces the electric potential at the top of the pores to −4.6 kV, whereas the potential is 3–4 kV higher beyond the edge of the SIWs. As the pore-chain tilts to the right at 22.5° and 45°, the micro-discharge in the gap tilts progressively to the left. There is a small asymmetry in the vacuum electric fields in the gap due to the spatially dependent permittivity below the surface, and this results in a small shift to the left of the initial streamer. However, the majority of the asymmetry is due to warping of the electric potential as the pore-chain fills with conductive plasma. The SIW on the top of the dielectric propagates to the left faster and with a higher electron density than the SIW propagating to the right. The slowing of the SIW to the right is likely a result of the surface capacitance C_s being larger to the right due to the orientation of the pore chain.

As the pore chain tilts to the right, the plasma coverage favors the lower surfaces of the pores. This directly translates to non-uniform fluxes of reactive species to the pore surfaces after the discharge pulse. The fluences of reactive species after 10 ns and 10 ms for the pore-chain oriented at 22.5° are shown in Fig. 10. The fluences of the pore chain oriented at 45° are shown in Fig. 11 (Fluences for the pore-chain oriented at 0° are shown in Fig. 4.). With the increasing angle of the pore-chain, the fluences at the end

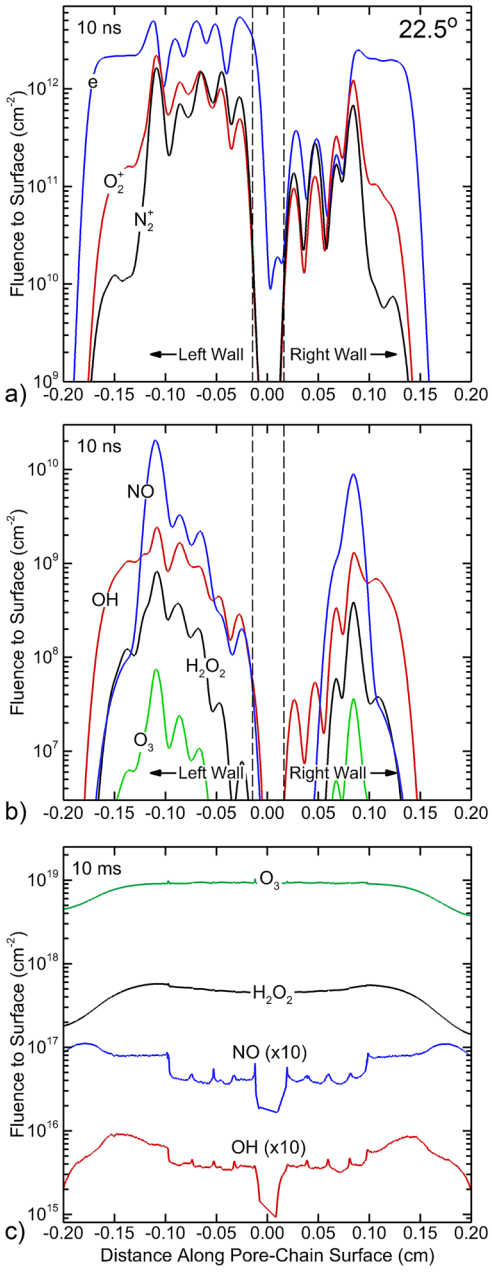

FIG. 10. Fluences of plasma-generated species to the inside surfaces of the pore-chain oriented at 22.5°. (a) Electrons and ions after 10 ns, (b) neutral species after 10 ns, and (c) neutral species after 10 ms. The maxima in fluences generally correspond to the pore openings. The dotted lines are the boundaries of the floor of the bottom pore.

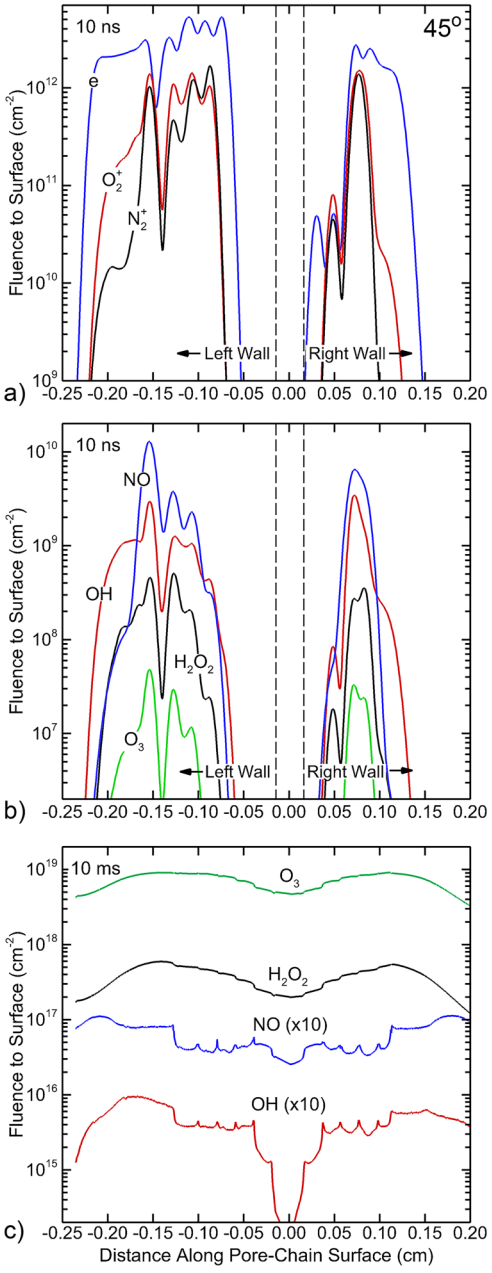

FIG. 11. Fluences of plasma-generated species to the inside surfaces of the pore-chain oriented at 45°. (a) Electrons and ions after 10 ns, (b) neutral species after 10 ns, and (c) neutral species after 10 ms. The maxima in fluences generally correspond to the pore openings. The dotted lines are the boundaries of the floor of the bottom pore.

of the discharge pulse at 10 ns for both the ions and neutrals increase on the left wall and decrease on the right wall. The deficit in fluences along the right wall near the bottom of the chain worsens with angle. This is in part due to the slower propagation speed of the SIWs over a longer distance. For the 45° orientation, the discharge fails to reach the bottom of the pore-chain by the end of the voltage pulse. The fluence of electrons is approximately an order of magnitude lower to the right-side wall compared to the fluence to the left-side all for a tilt of 22.5°. This disparity increases to approximately two orders of magnitude for a tilt of 45°.

After 10 ms, diffusion of the neutral species has in large part mediated the non-uniform fluences to surface produced by the angled pore chains. However, there is a limit (at least on these time scales) to this mediating diffusion. With the plasma not having fully reached the bottom of the pore chain for the 45° orientation, there are few neutral radicals produced in the bottom pore. As a result, there is a deficit of neutral reactive fluence to the walls of the bottom pore. Either the radical is depleted by the gas phase or surface reactions before diffusing to the last pore, which is the case for OH and NO, or there has not been enough time for the stable species (O_3 and H_2O_2) to diffuse through the chain.

VI. CONCLUDING REMARKS

The propagation of atmospheric-pressure plasmas into and through chains of dielectric pores (150 μm diameter) was computationally investigated. These pores are of the size typically found in materials used for tissue engineering and which often require functionalization of their surfaces for biocompatibility. The propagation of plasma into pores and pore-to-pore typically relies on photoionization to seed electrons in regions of high electric field. For pore-chains that are oriented parallel to the applied electric field, the polarization of the dielectric below the openings then avalanche these seed electrons to form micro-streamers that cross the majority of the pore diameter. Upon intersection with and charging of the surfaces of the pores, surface ionization waves (SIWs) then propagate along the walls of the pores.

The size of the openings between pores significantly impacts the method of plasma formation and propagation of plasma through the pore-chain. With small pore openings, photoionization is generally required to seed electrons in the next pore. The electric field enhancement at the edges of the openings then launches micro-streamers through the volume that in turn initiate SIWs. As the size of the openings increases, photoionization becomes less necessary to propagate the plasma as convective transport through the opening is less restricted. There is also less geometrical electric field enhancement due to the less sharp edges of the opening, and it is this electric field enhancement that typically launches volume micro-streamers. As a result, SIWs begin to dominate. With SIWs dominating, the fluences of reactive species become increasingly more uniform along the pore walls.

The angle of the pore-chain with respect to the applied electric field has a significant impact on plasma formation and uniformity of the fluence of ions and radicals to the inside surfaces of the pores. Even with a vertically oriented pore-chair, the fluence of ions to the pore surfaces is non-uniform due to the electric field enhancement at the pore openings and the mix of volumetric micro-streamers and SIWs in the pores. This non-uniformity is, however, symmetric on both sides of the pore-chain. As the angle of the pore-chain increases, the enhancement of the electric field at the pore openings becomes more pronounced, leading to the formation of high density microdischarges that launch SIWs on the lower surfaces of the pore-chains. There is little plasma directly formed on the upper surfaces, leading to non-uniform fluences of plasma-generated species to the two sides of the pore at the end of the discharge pulse. Non-uniformities in the fluences of charged species generally do not significantly improve during the afterglow following the discharge pulse. Diffusion of neutral species during the afterglow does improve the uniformity of their fluences to pore surfaces. Given the random orientation of pore-chains in most porous materials, obtaining uniform surface functionalization that requires a large ion component will be challenging. It will be far less challenging to obtain uniform surface functionalization that is dominated by neutral species, though several hundred to thousands of discharge pulses will be required to fully functionalize the surfaces.

Pore chains in industrial and biomedical materials have three-dimensional (3D) features that are not captured in the results from the two-dimensional (2D) simulations discussed here. Although we hesitate to comment quantitatively on how these 3D effects manifest themselves in plasma propagation through pore chains, as these simulations have not been done, we can make general comments. The electric field enhancement that results from sharp edges having the same radius of curvature are typically larger in 3D than in 2D and larger in a cylindrically symmetric structure that is off-axis than the equivalent Cartesian representations. In this regard, we expect that plasma propagation that relies on geometric electric field enhancement will be more intense in 3D. These features would include the micro-streamers that are launched from the edges of pore-openings in tilted pore chains. The solid angle subtended by a pore-opening in 3D is smaller than in 2D for otherwise equivalent dimensions. As a result, convective plasma transfer from pore-to-pore would likely be even more restricted in 3D compared to 2D. This increase in restriction would then make the contributions of photoionization to propagating the plasma pore-to-pore even more important in 3D.

ACKNOWLEDGMENTS

This material was based upon work supported by the U.S. Department of Energy, Office of Science, Office of Fusion Energy Sciences under Award Nos. DE-SC000319 and DE-SC0020232 and the National Science Foundation (Nos. PHY-1902878 and IIP-1747739).

DATA AVAILABILITY

The data that support the findings of this study are available from the corresponding author upon reasonable request.

REFERENCES

[1]A. Bogaerts, X. Tu, J. C. Whitehead, G. Centi, L. Lefferts, O. Guaitella, F. Azzolina-Jury, H. Kim, A. B. Murphy, W. F. Schneider, T. Nozaki, J. C. Hicks, A. Rousseau, F. Thevenet, A. Khacef, and M. Carreon, J. Phys. D: Appl. Phys. **53**, 443001 (2020).

[2]P. J. Bruggeman, M. J. Kushner, B. R. Locke, J. G. E. Gardeniers, W. G. Graham, D. B. Graves, R. C. H. M. Hofman-Caris, D. Maric, J. P. Reid, E. Ceriani, D. Fernandez Rivas, J. E. Foster, S. C. Garrick, Y. Gorbanev, S. Hamaguchi, F. Iza, H. Jablonowski, E. Klimova, J. Kolb, F. Krcma, P. Lukes, Z. Machala, I. Marinov, D. Mariotti, S. Mededovic Thagard, D. Minakata, E. C. Neyts, J. Pawlat, Z. Lj Petrovic, R. Pflieger, S. Reuter, D. C. Schram, S. Schröter, M. Shiraiwa, B. Tarabová, P. A. Tsai, J. R. R. Verlet, T. Von Woedtke, K. R. Wilson, K. Yasui, and G. Zvereva, Plasma Sources Sci. Technol. **25**, 053002 (2016).
[3]H. Kim, Y. Teramoto, A. Ogata, H. Takagi, and T. Nanba, Plasma Chem. Plasma Process. **36**, 45 (2016).
[4]C. Shuai, G. Liu, Y. Yang, W. Yang, C. He, G. Wang, Z. Liu, F. Qi, and S. Peng, Colloids Surf. B Biointerfaces **185**, 110587 (2020).
[5]A. Lipovka, R. Rodriguez, E. Bolbasov, P. Maryin, S. Tverdokhlebov, and E. Sheremet, Surf. Coat. Technol. **388**, 125560 (2020).
[6]A. Eltom, G. Zhong, and A. Muhammad, Adv. Mater. Sci. Eng. **2019**, 3429527.
[7]H. H. Kim, Y. Teramoto, A. Ogata, H. Takagi, and T. Nanba, Plasma Process. Polym. **14**, 1600157 (2016).
[8]H. H. Kim and A. Ogata, Eur. Phys. J. Appl. Phys. **55**, 13806 (2011).
[9]P. Mehta, P. Barboun, D. B. Go, J. C. Hicks, and W. F. Schneider, ACS Energy Lett. **4**, 1115 (2019).
[10]P. Mehta, P. Barboun, F. A. Herrera, J. Kim, P. Rumbach, D. B. Go, J. C. Hicks, and W. F. Schneider, Nat. Catal. **1**, 269 (2018).
[11]E. C. Neyts, K. K. Ostrikov, M. K. Sunkara, and A. Bogaerts, Chem. Rev. **115**, 13408 (2015).
[12]Z. Bo, S. Yang, J. Kong, J. Zhu, Y. Wang, H. Yang, X. Li, J. Yan, K. Cen, and X. Tu, ACS Catal. **10**, 4420 (2020).
[13]H. Amani, H. Arzaghi, M. Bayandori, A. S. Dezfuli, H. Pazoki-Toroudi, A. Shafiee, and L. Moradi, Adv. Mater. Interfaces **6**, 1900572 (2019).
[14]B. P. Chan and K. W. Leong, Eur. Spine J. **17**, 467 (2008).
[15]H. Rebl, B. Finke, J. Schmidt, H. S. Mohamad, R. Ihrke, C. A. Helm, and J. B. Nebe, Mater. Sci. Eng. C **69**, 1116 (2016).
[16]M. Wang, Y. Zhou, D. Shi, R. Chang, J. Zhang, M. Keidar, and T. J. Webster, Biomater. Sci. **7**, 2430 (2019).
[17]G. Lutzweiler, J. Barthes, G. Koenig, H. Kerdjoudj, J. Mayingi, F. Boulmedais, P. Schaaf, W. Drenckhan, and N. E. Vrana, ACS Appl. Mater. Interfaces **11**, 19819 (2019).
[18]M. Gherardi, R. Tonini, and V. Colombo, Trends Biotechnol. **36**, 583 (2018).
[19]X. Qiao, Y. M. Wang, W. X. Weng, B. L. Liu, and Q. Li, Ceram. Int. **44**, 21564 (2018).
[20]C. X. Wang, M. Du, and Y. P. Qiu, Surf. Coat. Technol. **205**, 909 (2010).
[21]Y. Sun, M. Krishtab, H. Struyf, P. Verdonck, S. De Feyter, M. R. Baklanov, and S. Armini, Langmuir **30**, 3832 (2014).
[22]J. Kim, S. A. Park, J. Kim, and J. Lee, Materials **12**, 1438 (2019).
[23]U. Roland, F. Holzer, and F. D. Kopinke, Appl. Catal. B Environ. **58**, 217 (2005).
[24]F. Holzer, U. Roland, and F. D. Kopinke, Appl. Catal. B Environ. **38**, 163 (2002).
[25]Y. Moriguchi, D. S. Lee, R. Chijimatsu, K. Thamina, K. Masuda, D. Itsuki, H. Yoshikawa, S. Hamaguchi, and A. Myoui, PLoS One **13**, e0194303 (2018).
[26]Y. Zhang, H. Y. Wang, Y. R. Zhang, and A. Bogaerts, Plasma Sources Sci. Technol. **26**, 054002 (2017).
[27]K. Hensel, V. Martišovitš, Z. Machala, M. Janda, M. Leštinský, P. Tardiveau, and A. Mizuno, Plasma Process. Polym. **4**, 682 (2007).
[28]S. Singh, C. Prakash, H. Wang, X. F. Yu, and S. Ramakrishna, Eur. Polym. J. **118**, 561 (2019).
[29]E. Simoncelli, D. Barbieri, R. Laurita, A. Liguori, A. Stancampiano, L. Viola, R. Tonini, M. Gherardi, and V. Colombo, Clin. Plasma Med. **3**, 77 (2015).
[30]A. Stancampiano, D. Forgione, E. Simoncelli, R. Laurita, R. Tonini, M. Gherardi, and V. Colombo, J. Adhes. Dent. **21**, 229 (2019).
[31]Y. R. Zhang, K. Van Laer, E. C. Neyts, and A. Bogaerts, Appl. Catal. B Environ. **185**, 56 (2016).
[32]Q. Z. Zhang and A. Bogaerts, Plasma Sources Sci. Technol. **27**, 035009 (2018).
[33]C. Swanson and I. D. Kaganovich, J. Appl. Phys. **123**, 023302 (2018).
[34]J. G. Gu, Y. Zhang, M. X. Gao, H. Y. Wang, Q. Z. Zhang, L. Yi, and W. Jiang, J. Appl. Phys. **125**, 153303 (2019).
[35]S. A. Norberg, E. Johnsen, and M. J. Kushner, Plasma Sources Sci. Technol. **24**, 035026 (2015).
[36]A. M. Lietz and M. J. Kushner, J. Phys. D: Appl. Phys. **49**, 425204 (2016).
[37]P. R. Prezas, B. M. G. Melo, L. C. Costa, M. A. Valente, M. C. Lança, J. M. G. Ventura, L. F. V. Pinto, and M. P. F. Graça, Appl. Surf. Sci. **424**, 28 (2017).
[38]J. P. Gittings, C. R. Bowen, I. G. Turner, A. C. E. Dent, F. R. Baxter, and J. Chaudhuri, Acta Biomater. **5**, 743 (2009).